The origin of optical emission lines in the soft state of X-ray binary outbursts: the case of MAXI J1820+070

K. I. I. Koljonen [1,2,3]★ K. S. Long,[4,5] J. H. Matthews [6] and C. Knigge [7]

[1]*Institutt for Fysikk, Norwegian University of Science and Technology, Høgskloreringen 5, Trondheim 7491, Norway*
[2]*Finnish Centre for Astronomy with ESO (FINCA), University of Turku, Vesilinnantie 5, 20014 Turku, Finland*
[3]*Aalto University Metsähovi Radio Observatory, PO Box 13000, FI-00076 Aalto, Finland*
[4]*Space Telescope Science Institute, 3700 San Martin Drive, Baltimore, MD 21218, USA*
[5]*Eureka Scientific Inc., 2452 Delmer Street, Suite 100, Oakland, CA 94602-3017, USA*
[6]*Department of Physics, Astrophysics, University of Oxford, Denys Wilkinson Building, Keble Road, Oxford, OX1 3RH, UK*
[7]*School of Physics and Astronomy, University of Southampton, Highfield, Southampton, SO17 1BJ, UK*

ABSTRACT
The optical emission line spectra of X-ray binaries (XRBs) are thought to be produced in an irradiated atmosphere, possibly the base of a wind, located above the outer accretion disc. However, the physical nature of – and physical conditions in – the line-forming region remain poorly understood. Here, we test the idea that the optical spectrum is formed in the transition region between the cool geometrically thin part of the disc near the mid-plane and a hot vertically extended atmosphere or outflow produced by X-ray irradiation. We first present a VLT X-Shooter spectrum of XRB MAXI J1820+070 in the soft state associated with its 2018 outburst, which displays a rich set of double-peaked hydrogen and helium recombination lines. Aided by ancillary X-ray spectra and reddening estimates, we then model this spectrum with the Monte Carlo radiative transfer code PYTHON, using a simple biconical disc wind model inspired by radiation-hydrodynamic simulations of irradiation-driven outflows from XRB discs. Such a model can qualitatively reproduce the observed features; nearly all of the optical emission arising from the transonic 'transition region' near the base of the wind. In this region, characteristic electron densities are on the order of $10^{12-13}\,\mathrm{cm}^{-3}$, in line with the observed flat Balmer decrement (H α/H $\beta \approx 1.3$). We conclude that strong irradiation can naturally give rise to both the optical line-forming layer in XRB discs and an overlying outflow/atmosphere that produces X-ray absorption lines.

Key words: Accretion, accretion discs – binaries: close – stars: individual: MAXI J1820+070 – stars: winds, outflows – X-rays: binaries.

1 INTRODUCTION

X-ray binaries (XRBs) are systems where a compact object accretes material from a non-degenerate companion star. The accreting gas exhibits a large range of temperatures and densities – primarily depending on the distance to the compact object – allowing us to study a wide variety of astrophysical plasmas in a single source. XRBs also drive outflows from their discs in the form of fast strongly collimated jets and slower less collimated disc winds (e.g. Fender, Belloni & Gallo 2004; Ponti et al. 2012). The disc winds are observationally more elusive than jets, but their mass-loss rate is larger and may occasionally even exceed the accretion rate. As a result, disc winds have the potential to severely affect the overall accretion flow (Muñoz-Darias et al. 2016; Casares et al. 2019). They might also extract angular momentum from the disc regulating the evolution of XRB outbursts (Tetarenko et al. 2018).

Evidence for equatorial disc winds has mostly been accumulated via X-ray spectroscopy obtained during outbursts in the form of blueshifted absorption lines associated with highly ionized absorbers

(Fe XXV K α/Fe XXVI Ly α; Díaz Trigo & Boirin 2016; Ponti et al. 2016, and references therein). Interestingly, these absorption lines are typically observed in the so-called soft X-ray state, during which the luminosity is dominated by thermal emission from the disc. However, they are rarely present during the so-called hard X-ray state, when non-thermal emission from a hot optically thin plasma dominates the X-ray spectrum and radio jets are observed (Miller et al. 2006; Neilsen & Lee 2009; Neilsen, Remillard & Lee 2011; Ponti et al. 2012; Ponti, Muñoz-Darias & Fender 2014). This has sparked discussion of whether the jets and winds exclude each other (Neilsen & Lee 2009), or whether they can coexist as seems to be the case at least in a few sources (Rahoui, Coriat & Lee 2014; Homan et al. 2016; Muñoz-Darias et al. 2016, 2017; Allen et al. 2018).

In addition to X-rays, evidence of disc winds has also been seen in optical spectra, most convincingly in the form of P-Cygni-like blueshifted broad absorption profiles associated with hydrogen and helium optical lines (Muñoz-Darias et al. 2016; Muñoz-Darias, Torres & Garcia 2018; Charles et al. 2019; Jiménez-Ibarra et al. 2019; Muñoz-Darias et al. 2019). Recently, similar disc wind signatures have also been detected in the profiles of *ultraviolet* resonance lines (Castro Segura et al. 2022). However, contrary to X-ray observations, these lower-energy wind signatures are seen preferentially during the

★ E-mail: karri.koljonen@ntnu.no (KIIK); long@stsci.edu (KSL)

hard state. This raises an interesting question of whether the disc wind is present throughout the outburst, but its properties change between the soft and hard states. Such changes could be associated with the disc geometry (Ueda et al. 2010; Miller et al. 2012; Ponti et al. 2012) and/or the ionization state of the wind (Jimenez-Garate et al. 2001; Ueda et al. 2010; Díaz Trigo et al. 2012; Chakravorty, Lee & Neilsen 2013; Díaz Trigo et al. 2014; Higginbottom & Proga 2015; Díaz Trigo & Boirin 2016; Bianchi et al. 2017).

MAXI J1820+070 (ASASSN-18ey) was first detected at the start of its outburst in early 2018 (Tucker et al. 2018) and became one of the brightest XRB outbursts ever observed, with an X-ray flux reaching ∼4 Crab and an optical magnitude reaching 11.2 (Shidatsu et al. 2019). However, as the source is relatively close by, 3.0 ± 0.3 kpc (Atri et al. 2020), the inferred peak luminosity was quite typical for an XRB outburst, at about 15 per cent of the Eddington luminosity. Since disc winds are preferentially detected in systems viewed more edge-on (Ponti et al. 2012; Higginbottom et al. 2020), the relatively high inclination inferred for MAXI J1820+070 – $i > 60$ deg (Atri et al. 2020; Torres et al. 2020) – makes it a promising target for observational studies aimed at these outflows. Indeed, clear accretion disc wind features (P-Cygni profiles and broad emission line wings) were observed in the hard state during both outburst rise and decay (Muñoz-Darias et al. 2019). In addition, wind features were found during the soft state in the infrared Pa γ and Pa β lines, indicating that the outflow was present throughout the outburst (Sánchez-Sierras & Muñoz-Darias 2020). Clear absorption lines in the X-ray spectra have not been found (partly because the outburst was too bright to be observed with *XMM-Newton* and *Chandra*), but some *NICER* soft state spectra show dips at ∼7 keV that can be fitted with an outflowing ionized absorber (Fabian et al. 2020).

Most of the optical studies on XRB accretion disc winds have concentrated on the effects of the wind on single lines in the form of P-Cygni profiles and broad emission line wings. By contrast, the blue continuum and double-peaked emission lines are usually taken to arise directly from the irradiated accretion disc. However, it is worth asking if the wind could affect the observed spectrum more generally, imprinting it with emission lines and an additional continuum component. This is especially important given the evidence that the disc wind is present at all times. Models like this have been explored in the context of accreting white dwarfs with promising results (e.g. Matthews et al. 2015). However, in XRBs, the optical continuum is typically described simply with a power-law model, while the lines are modelled individually.

In this paper, we study the possible effect of a disc wind – or, more generally, an extended disc atmosphere – on the UV, optical, and infrared (UVOIR) spectrum of MAXI J1820+070 during the soft state of its outburst. The underlying irradiating continuum is estimated by modelling quasi-simultaneous multiwavelength observations obtained by ESO's Very Large Telescope (VLT), *Swift*, *NICER*, and *NuSTAR*. We then use PYTHON, a Monte Carlo ionization and radiative transfer code to reproduce the observed line spectrum and to derive the physical parameters of the disc wind/atmosphere.

2 OBSERVATIONS

We carried out a multi-epoch observing campaign with VLT/X-Shooter covering the 2018 outburst of MAXI J1820+070. In this paper, we consider only one epoch of this campaign, which coincided with the soft state. During this epoch, the broad-band spectrum was dominated mainly by a thermal disc component (Fig. 1).

In addition, we analysed UV and X-ray pointed observations taken at approximately the same time as the X-Shooter data, allowing us to construct a full spectral energy distribution (SED).
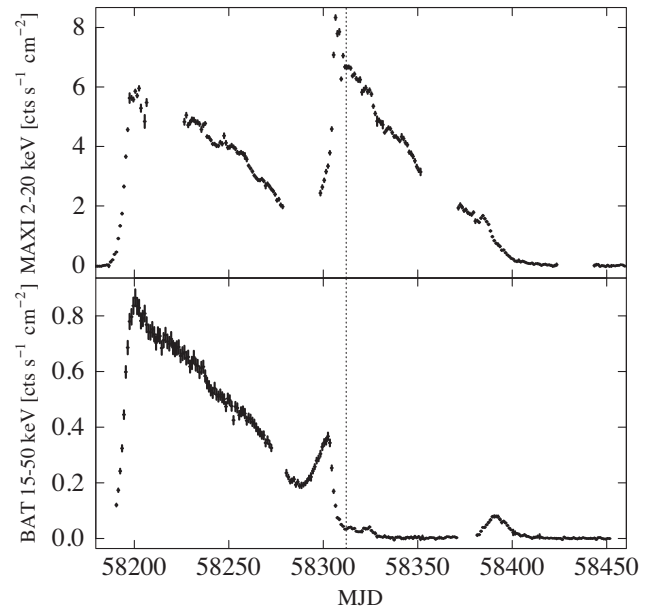

Figure 1. *MAXI*/GSC and *Swift*/BAT light curves of MAXI J1820+070. The time of the X-Shooter observation taken after the change from the hard state to the soft state is marked with a dotted line.

We downloaded *Swift*, *NICER*, and *NuSTAR* pointing observations from the High Energy Astrophysics Science Archive Research Center (HEASARC) that were as close as possible to the time of the X-Shooter observation.

2.1 X-Shooter

The X-Shooter observation considered here was obtained during the soft state starting on MJD 58312.118 (2018-07-13 02:50). The observation consisted of four exposures of ∼10 min each, arranged in AB pairs alternating between source and sky positions. We used a nod throw length of five arcseconds and a jitter box of one arcsecond. The total observing time, including overheads, was ∼45 min.

The slit acquisition was carried out with the '*i*'-band filter, which we also used to correct the flux level of the X-Shooter spectra due to slit losses. The '*i*'-band magnitude of MAXI J1820+070 was 13.0 without correcting for the interstellar reddening. The slit widths used were 1.3, 1.3, and 1.2 arcsec for UV, VIS, and NIR arms, respectively. The readout mode of the detector was 100 k/1pt/hg/1x2. We reduced the X-Shooter data with the ESO pipeline v3.5.0 in ESOREFLEX. The telluric absorption was corrected using MOLECFIT (Smette et al. 2015).

To facilitate the broad-band continuum fitting presented in Section 3.3, we formed a line/edge-free continuum spectrum by selecting first only continuum regions from the X-Shooter spectrum and interpolating over the line/edge regions. We binned the spectrum to 100 logarithmically spaced wavelength bins and assumed a 5 per cent error for each data point.

2.2 *Swift*/UVOT

There were two *Swift* pointed observations of MAXI J1820+070 on the date of the X-Shooter observation: pointing 00 010 754 003 with observation start time MJD 58312.208 (2018-07-13 05:00) and pointing 00 010 754 004 with observation start time MJD 58312.341 (2018-07-13 08:11). While the closest *Swift* observation to the X-Shooter data was pointing 00010754003, it contained only one

Table 1. *Swift*/UVOT photometry of MAXI J1820+070 on 2018-07-13. The magnitudes and fluxes correspond to reddened values.

Filter	Freq. [10^{14} Hz]	Exp. [s]	Mag. [mJy]	Flux [mJy]	Err. [mJy]
V	5.55	135	12.99	23.0	0.7
U	8.56	135	13.12	20.8	0.8
UW1	11.6	270	13.48	14.5	0.7
UM2	13.5	229	13.76	11.4	0.4
UW2	14.8	540	13.65	12.5	0.6

UVOT exposure (taken in the *U* band). We therefore chose to use the second pointing, obtained three hours later, which contained exposures in five *UVOT* bands: *V*, *U*, *UW1*, *UM1*, and *UW2*. The *U*-band magnitudes were consistent at both pointings.

The magnitudes and flux densities of MAXI J1820+070 were calculated using the UVOTSOURCE task in HEASOFT 6.26.1 for each filter. For extracting the source counts, we used a circular aperture with a radius of five arcseconds centred on the location of the source (RA 18:20:21.4, Dec. +07:10:53.1). The background was estimated using a circular source-free aperture with a radius of 12 arcsec located close to MAXI J1820+070. Table 1 shows the results from the photometry.

2.3 *NuSTAR*

The *NuSTAR* observation closest to the X-Shooter data in time was pointing number 0401309025, with an observation start time of MJD 58314.744 (2018-07-15 17:51). While this observation was taken ∼2.5 d later, the *MAXI*/GSC and *Swift*/BAT count rates remained consistent across these dates, so we do not expect any significant change in the X-ray spectral shape or normalization. Adding the *NuSTAR* data to the broad-band spectral energy distribution provides essential constraints on the amount of hard X-ray emission and the irradiation of the accretion disc.

We reduced the *NuSTAR* data from the two focal plane modules (FPMA and FPMB) using the NUPIPELINE task contained in HEASOFT 6.26.1. We used a circular source region with a 160 arcsec radius centred on the location of the source. We estimated the background using a circular aperture with a 160 arcsec radius located in a source-free region of the image. We ran the pipeline with the parameters TENTACLE = 'YES' and SAAMODE = 'OPTIMIZED'. The former requires a simultaneous increase in the CdZnTe detector event count rates and the observed shield single rates, while the latter allows identification and flagging of time intervals in which the CdZnTe detector event count rates show an increase when the spacecraft enters the South Atlantic Anomaly (SAA).

We extracted averaged spectra from the two detectors with the task NUPRODUCTS contained in HEASOFT 6.26.1. The broad-band (3–79 keV) *NuSTAR* count rate ranged between 490–530 cts s^{-1}. For X-ray modelling, we binned the data to a minimum signal-to-noise ratio (S/N) of 30 across the full 3–79 keV band.

2.4 *NICER*

The *NICER* pointing closest in time to the *NuSTAR* data set was obsid 1 200 120 207 and took place on MJD 58314.181 (2018-07-15 04:20). The on-source exposure time was 4.6 ksec.

We reduced the observation using NICERDAS version 10, using the NICERL2 script with default parameters. We extracted the X-ray spectra and accompanying detector response files using the NICERL3-SPECT script and opted for SCORPEON (version 22) background modelling. For the spectral analysis, we binned the data to S/N

= 30. We performed spectral fitting using the Interactive Spectral Interpretation System (ISIS; Houck 2002) and estimated the errors on the best-fitting parameter values via Monte Carlo analysis. In the modelling, we added a constant factor to account for the flux difference between the X-ray detectors.

3 RESULTS

3.1 Line spectrum

The X-Shooter spectrum is rich in optical and infrared emission lines, as shown in Fig. 2. The underlying continuum rises towards the UV, as expected for emission produced by an accretion disc. The spectrum shows a remarkable collection of emission features, most of which correspond to recombination lines associated with hydrogen and helium. For example, the Balmer, Paschen, and Brackett series of hydrogen are all identifiable, down to transitions 10–2, 18–3, and 18–4, respectively. The corresponding photoionization edges are also visible and are observed in emission. This immediately implies that there is a significant recombination continuum contribution to the broad-band optical SED. Evidently, the material responsible for generating the emission lines also affects the overall continuum shape.

All of the hydrogen lines are double-peaked, except Pa β and Pa γ, which display a weaker third peak in the blue line wing. The line profile of all hydrogen lines is relatively uniform, with the blue peak being more substantial. The only exceptions are the higher-order Balmer transitions, which show peaks of roughly equal strength.

In addition to the hydrogen lines, several helium emission lines are also visible, notably He I λ10830 and He II λ4686. Weaker helium lines can be found in He I λ4026, He I λ4388, He I λ4471, He I λ4922, He I λ5016, He I λ5048, He I λ5876, He I λ6678, He I λ7065, He I λ7281, He I λ11969, He I λ17002, He II λ5412, He II λ10124, and He II λ11626. The shapes of the helium lines mirror those of the hydrogen lines in displaying stronger blue peaks.

Two prominent Bowen fluorescence features are also visible: O III λ3444 and the O III/N III blend near λ4650. The formation of these features requires a strong extreme-UV source, so their presence is consistent with our observation in the soft state (cf. Fig. 3). In addition, the Ca II H&K lines are observed both in emission and absorption (with the absorption likely being produced in the interstellar medium).

Two emission lines escaped our classification that are located at roughly λ6338 and λ7762. We also identify several diffuse interstellar band (DIB) lines in the X-Shooter spectra, centred at λ5780, λ5797, λ6202, λ6270, and λ6284.

3.2 Reddening

It is important to adopt appropriate estimates of extinction (A_V) and reddening (E_{B-V}) when modelling optical data. As discussed in more detail below, three different methods suggest $E_{B-V} \simeq 0.2$ for MAXI J1820+070. We adopt the standard value of $R_V = A_V/E_{B-V} = 3.1$ throughout our analysis.

3.2.1 HI column density

Extinction and reddening are strongly correlated with neutral atomic hydrogen column density (N_H) along any given line of sight (e.g. Bohlin, Savage & Drake 1978; Friedman et al. 2011; Liszt 2014). In the case of MAXI J1820+070, N_H can be obtained from 21-cm radio observations by fitting the interstellar absorption of the
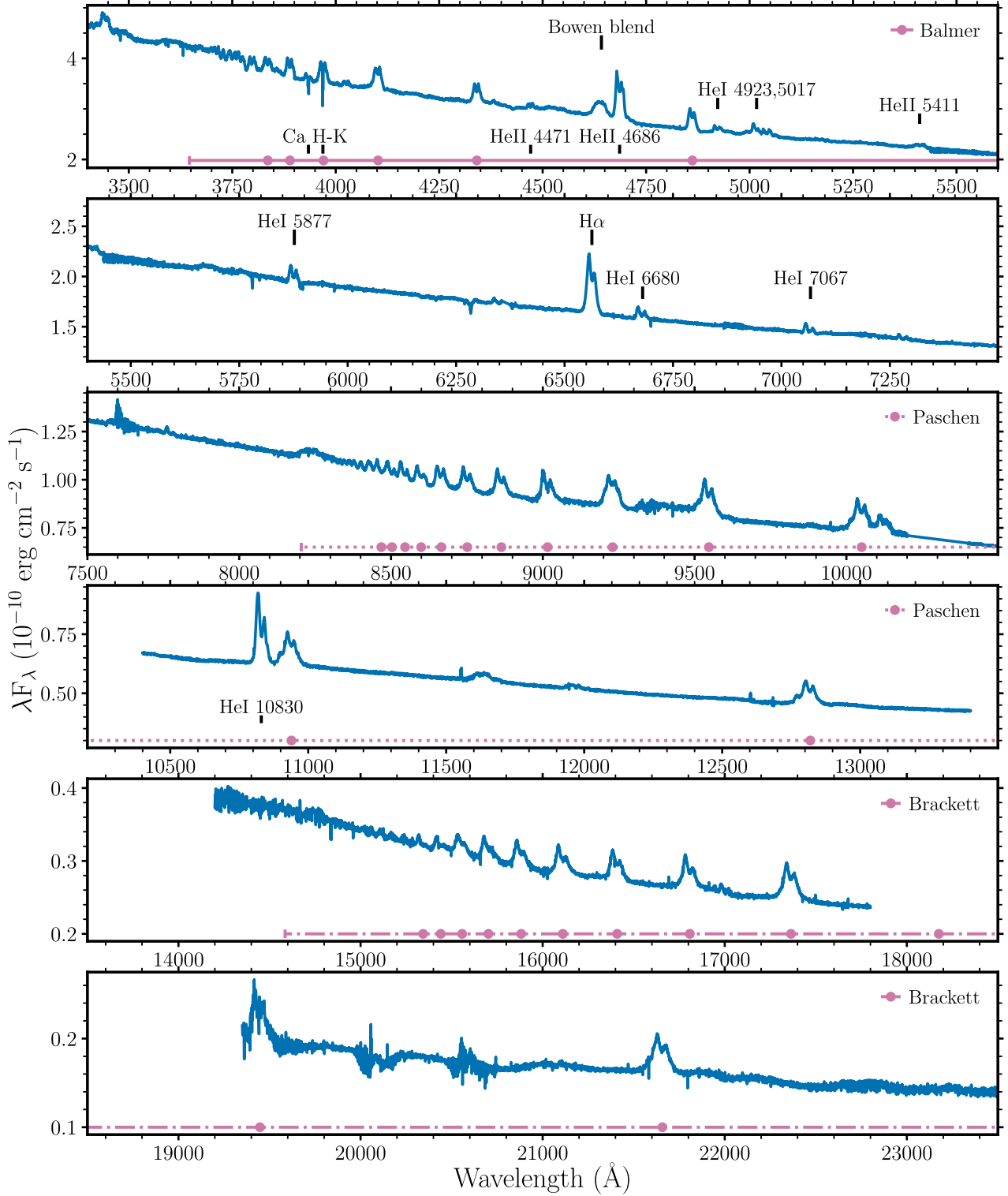
Figure 2. The dereddened optical-to-near-infrared spectrum obtained with X-Shooter shows a rich emission line spectrum and blue continuum. Prominent emission lines are marked, and the Balmer, Paschen, and Brackett series of Hydrogen emission lines are labelled with pink dots.

X-ray spectrum and by measuring the equivalent widths of diffuse interstellar bands (DIBs).[1]

---

[1]We use DIB EWs to estimate $N_{\rm H}$, rather than E_{B-V}, since the former correlation is much tighter (Friedman et al. 2011).

First, HI4PI Collaboration et al. (2016) provide an estimate of 1.3×10^{21} atoms cm^{-2} in the direction of MAXI J1820+070 based on the high-resolution 21-cm radio observations. Second, in Section 3.3, we fit the absorbed X-ray spectrum using an interstellar absorption model TBNEW with elemental abundances from Wilms, Allen & McCray (2000). This analysis yields an estimate of $N_{\rm H}$
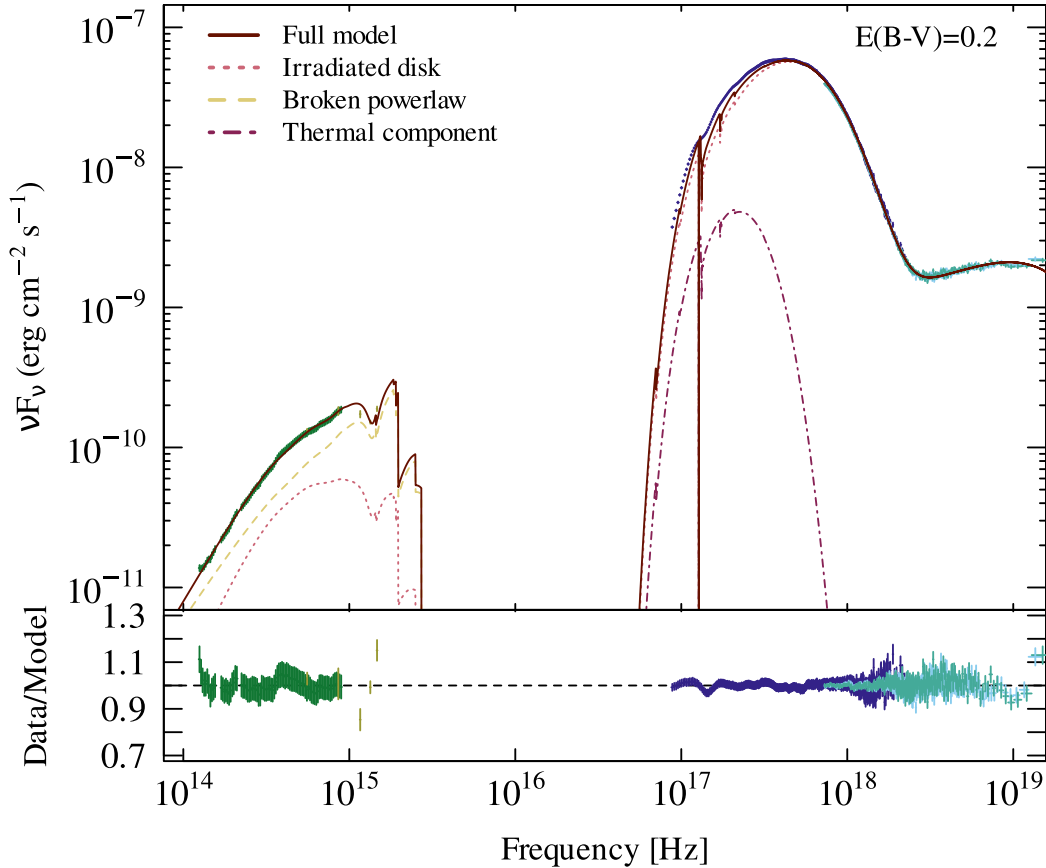
Figure 3. Broad-band data fitted with the model described in Section 3.3. Dark green: X-Shooter data, light green: *Swift*/UVOT data, dark blue: *NICER* data, light blue: *NuSTAR* data, solid curve: full absorbed model as tabulated in Table 3, dotted curve: disc irradiation component, dashed curve: broken power law in the UVOIR region (possibly a component arising from the wind/disc atmosphere), dot–dashed curve: 'soft excess' (possibly a component arising from the wind/disc atmosphere).

$= 1.3 \times 10^{21}$ atoms cm^{-2}. Third, we have estimated the equivalent width of the $\lambda 5780$ line in our X-Shooter data from a Voigt profile fit. This yielded EW($\lambda 5780$) $= 0.188$ Å, which, based on the correlation between EW and NH established by Friedman et al. (2011), suggests a value of $N_H = 1.4 \pm 0.4 \times 10^{21}$ atoms cm^{-2}. Thus all three methods yield similar values of N_H.

The reddening can then be estimated from N_H via the N_H/E_{B-V} relation (Bohlin et al. 1978; Liszt 2014). Assuming a conversion of $N_H/E_{B-V} = 8.3 \times 10^{21}$ cm^{-2} mag^{-1} at$|b| < 30°$(Liszt 2014), the implied E_{B-V} is 0.17. This is somewhat less than would be derived from the often quoted relationship of $N_H = 5$–6×10^{21} cm^{-2} mag^{-1} (Bohlin et al. 1978), which would lead to E_{B-V} between 0.23 and 0.28.

3.2.2 Dust maps

We can also estimate the reddening and extinction towards MAXI J1820+070 from models of the Galactic dust distribution. We used the GALExtin service (Amôres et al. 2021) for this purpose, which provides convenient access to several such models.[2] For the distance

and direction of MAXI J1820+070 the model of Amôres & Lépine (2005) gives $A_V = 0.59$ mag. For our standard value of $R_V = A_V/E_{B-V} = 3.1$, this corresponds to $E_{B-V} = 0.19$. Similarly, the model of Drimmel, Cabrera-Lavers & López-Corredoira (2003) gives $E_{B-V} = 0.22$, Schlafly et al. (2014) and Planck Collaboration XI (2014) both suggest $E_{B-V} = 0.25$, and the model of Green et al. (2018) yields $E_{B-V} = 0.17$. Thus dust models also suggest a value of $E_{B-V} \simeq 0.2$ for MAXI J1820+070.

3.2.3 The 2200 Å feature

A final reddening estimate can be obtained from the ultraviolet continuum shape. During its outburst, we observed MAXI J1820+070 twice with the *Hubble Space Telescope*, providing two epochs of far- and near-ultraviolet spectroscopy. A complete analysis of the resulting data will be presented separately (Georganti et al., in preparation), but the strength of the well-known 2200 Å dust absorption feature in these observations also suggests $E_{B-V} \simeq 0.2$.

3.3 Broad-band continuum

In the soft state of XRBs, the X-ray spectrum is dominated by a thermal component peaking around 1 keV. The thermal component

---

[2]It should be acknowledged here that these dust model estimates cannot be considered strictly independent since the models tend to be calibrated with the same core data sets. Moreover, some models – e.g. the Amôres & Lépine (2005) one – are at least partially calibrated via H I observations. Such resulting estimates are therefore also not strictly independent of those obtained in Section 3.2.1. Nevertheless, it is at least somewhat reassuring that

the dust model estimates are consistent both with each other and with the N_H-based estimates.

Table 2. System parameters of MAXI J1820+070 found in the literature. We adopt an inclination of 65° and $M_{BH} = 8.5\,M_\odot$ in our modelling.

Parameter	Unit	Value	Ref.
Distance	kpc	2.96 ± 0.33	1
Jet inclination	deg	63 ± 3	1
Orbital inclination	deg	$62 < i < 81$	2
M_{BH} (jet)	$M_\odot$	$8.5^{+0.8}_{-0.7}$	2
M_{BH} (orbit)	$M_\odot$	$6.0 < M_{BH} < 8.1$	2
q		0.072 ± 0.012	2

Note. References: (1) Atri et al. (2020), (2) Torres et al. (2020).

is typically accompanied by a weak hard Compton tail extending to higher energies. These components are often interpreted as arising, respectively, from a thermal, multicolour accretion disc and a non-thermal, optically thin region possibly associated with reconnection sites above the thermal disc (Haardt, Maraschi & Ghisellini 1994) or with a small 'corona' close to the black hole. In addition to the canonical disc and non-thermal component, an additional thermal component is needed to fit the soft state X-ray spectrum of MAXI J1820+070. This has been suggested to arise from a plunge region close to the black hole (Zhu et al. 2012; Fabian et al. 2020). On the other hand, similar thermal components have been reported before from other XRBs (Życki, Done & Smith 2001; Chiang et al. 2010; Shaw et al. 2016), and another possibility for it could be inner disc irradiation or enhanced dissipation in the upper layers of the disc (Davis et al. 2005; see also discussion in Done et al. 2012).

During XRB outburst soft states, the strongest component in the UVOIR spectral region likely arises from the irradiated outer disc illuminated by the X-ray emission emanating from close to the black hole. The optical emission from the companion star is also much weaker, by several orders of magnitude (Torres et al. 2020). Typically, the viscous disc spectrum in the UVOIR is a power law with an index close to $\beta = 1/3$; $F_\nu \propto \nu^\beta$.

To model the full spectral energy distribution from UVOIR to X-rays, we use the irradiated disc model OPTXRPLIR (Shidatsu, Done & Ueda 2016; Kimura & Done 2019). The model assumes that the irradiating X-ray flux scales with the radius as $r^{-12/7}$ and that the irradiating flux consists of the canonical thermal disc contribution, an additional soft thermal Comptonization component, and a non-thermal (power law) component. The non-thermal component is assumed to be located close to the compact object from the innermost stable orbit to a radius R_{pl}, while the soft thermal Comptonization component is located between R_{pl} and a radius R_{comp}. The non-thermal component is parametrized with a power law index Γ_{pl}, while the thermal Comptonization component is controlled by an electron temperature kT_e and an optical depth τ. The irradiated, multicolour disc is characterized by an inner disc temperature kT_{bb}, and is assumed to be located between R_{comp} and the outer disc edge, R_{out}.

Since the orbital parameters of the system are quite well determined, we restricted the outer disc radius to lie between the circularization radius,

$$\frac{R_{circ}}{a} = 0.074 \left(\frac{1+q}{q^2}\right)^{0.24} \approx 0.27, \tag{1}$$

and tidal radius

$$\frac{R_{tidal}}{a} = 0.112 + \frac{0.27}{1+q} + \frac{0.239}{(1+q)^2} \approx 0.57. \tag{2}$$

Here, $q = M_2/M_{BH} = 0.072 \pm 0.012$ (Torres et al. 2020; Table 2) is the mass ratio and $a \sim 4.5 \times 10^{11}$ cm is the orbital separation. The

resulting limits on the outer disc radius are $10^{4.8} r_g \leq R_{out} \leq 10^{5.4} r_g$, where r_g is the gravitational radius.

The irradiation efficiency in the OPTXRPLIR model is parametrized as the fraction of illuminating flux thermalized in the outer disc. This is given by $F_{out} = f_{out}(1 - a_{out})$, where f_{out} is the height of the disc at the outer edge divided by the outer radius and a_{out} is the albedo of the outer disc. We fix the albedo to a value of $a_{out} = 0.9$, which corresponds to a highly ionized and reflective disc surface and is typical for soft-state XRBs (van Paradijs & McClintock 1994; Jimenez-Garate, Raymond & Liedahl 2002; Gierliński, Done & Page 2009).

The normalization of this disc model depends on several physical parameters: the mass of the black hole (M_{BH}), the total luminosity (L), the black hole spin, the disc inclination (i), and the distance to the source (d). In our modelling, we adopt $M_{BH} = 8.5\,M_\odot$, $i = 65°$, and $d = 3$ kpc, as shown in Table 2. In addition, we assume a non-spinning black hole (Guan et al. 2021; Zhao et al. 2021). We also adopted solar abundances for all elements taken from Wilms et al. (2000).

When we applied this model to the X-ray data – also allowing for interstellar absorption by adding TBNEW[3] as a multiplicative component – we found that unacceptable residual remained in the soft X-ray region. We therefore added a (relatively) low-temperature and low-normalization black body component ($kT_{bb} \sim 0.2$ keV).[4] This component could potentially arise from the reprocessed emission lines in the illuminated disc atmosphere or wind base (see Section 4.2.2). Thus, we fit the X-ray spectrum with the ISIS parametrization CONSTANT × TBNEW × (OPTXRPLIR + BBODY). This model yielded acceptable fits to the X-ray region.

We then extended the data range considered to include the longer-wavelength UVOT and X-Shooter data. As a starting point, we fitted the above model to the whole broad-band spectrum, but now also including an interstellar reddening component with $E_{B-V} = 0.2$ (see Section 3.2). However, this model could not be fully reproduce the X-Shooter continuum, primarily because it underpredicts the infrared flux. Since the observation is taken in the soft state, it is unlikely that the required extra emission component arises from a jet or a companion star. However, as we show below in Section 4.2, the reprocessing in a wind or an atmosphere above the disc can produce infrared continuum emission comparable to that from an irradiated outer disc.

In order to first obtain a rough approximation of the overall spectrum, we added a broken power-law component to account for the infrared flux deficit. We fixed the break frequency to 0.04 keV and the power law photon index after the break to $\Gamma = 5$, leaving the photon index before the break and the normalization as free parameters. Thus, the final model fitted to the overall broad-band SED is CONSTANT × REDDEN × TBNEW × (OPTXRPLIR + BKN-POWER + BBODY). The best-fitting model is shown in Fig. 3, and the parameters are tabulated in Table 3.

The above model produced a good fit ($\chi^2_{red} \sim 0.9$) with the largest residuals arising in the very soft end of the *NICER* spectrum and in the optical and UV region. The soft X-ray residuals could arise either from a calibration issue, insufficient modelling of the soft X-ray absorption, or the effect of additional absorption/emission lines. The fitted value of the interstellar absorption is $N_H \sim 1.3 \times 10^{21}$ cm^{-2}, though, in line with the estimates from other methods described in Section 3.2. The residuals in the optical/UV most likely arise from the insufficient modelling of the Paschen edge and possible differences

---

[3]An updated version of TBABS (Wilms et al. 2000).
[4]We also experimented with letting the abundances of the absorption component vary instead of adding the blackbody component, but this did not produce good enough results.

Table 3. Full SED model parameters.

CONSTANT × REDDEN × TBNEW × (OPTXRPLIR + BKNPOWER + BBODY)				
TBNEW	N_H			
	$(10^{20}\,\mathrm{cm}^{-2})$			
	12.95 ± 0.19			
OPTXRPLIR	L	kT_{bb}	r_{pl}	Γ_{pl}
	(L_{Edd})	(keV)	(R_g)	
	0.1266 ± 0.0002	1.00 ± 0.01	$8.98^{+0.05}_{-0.04}$	1.70 ± 0.01
	r_{comp}	kT_e	τ	f_{out}	$\log r_{out}$
	(R_g)	(keV)			(R_g)
	17.2 ± 0.5	20.5 ± 2	7.8 ± 0.1	0.013 ± 0.004	5.29 ± 0.06
BKNPOWER	norm	β			
	5170^{+1989}_{-1244}	$0.19^{+0.04}_{-0.06}$			
BBODY	norm	kT_{bb}			
		(keV)			
	0.130 ± 0.007	0.187 ± 0.004			

Notes. Fit quality: $\chi^2/\mathrm{d.o.f.} = 1147/1281$; $\chi^2_{red} = 0.90$,
Fixed parameters: $\theta_{inc} = 65$ deg; $M_{BH} = 8.5\,\mathrm{M}_\odot$; $d = 3$ kpc; $a_* = 0$; $a_{out} = 0.9$; $E_{B-V} = 0.2$.

to the assumed extinction law (REDDEN uses the extinction law from Cardelli, Clayton & Mathis 1989).

4 MODELLING THE EMISSION LINE SPECTRUM

In order to gain insight into the nature of the gas that produces the emission features in the X-Shooter spectrum of MAXI J1820+070, we have modelled the spectrum with the Monte Carlo radiative transfer (MCRT) and ionisation code, PYTHON. The code and the kinematic model it uses are described in more detail in Section 4.1, and the results of our modelling effort are described in Section 4.2.

As we shall see, the dense, cool, and quasi-static base of a thermally driven disc wind can provide a suitable environment for forming the observed optical spectrum. However, it is important to note from the outset that we are *not* claiming that the presence of the wind is crucial to our ability to reproduce the observations. Instead, *any* irradiated layer above the disc with physical conditions similar to those we find in our wind base would likely produce a similar spectrum.

Our choice to describe this region as the base of a thermally driven wind is based on two considerations. First, such a wind is theoretically expected to be present in any system where a sufficiently large disc is subject to strong irradiation (e.g. Begelman, McKee & Shields 1983; Woods et al. 1996; Proga & Kallman 2002; Higginbottom et al. 2019), and – as discussed in Section 1 – observational signatures of disc winds have indeed been seen in many luminous XRBs. It is therefore natural to ask whether/how such a wind might also produce the observed optical emission lines. Second, PYTHON is a code designed to model outflows. Thus the density and velocity fields across the numerical grid are (usually) set-up by specifying the parameters of a simple biconical disc wind (e.g. the mass-loss rate, the outflow opening angles, and the poloidal velocity law).

4.1 Monte Carlo radiative transfer modelling

PYTHON was originally developed by Long & Knigge (2002).[5] It has also been used by Higginbottom et al. (2018, 2020) in their radiation-hydrodynamic simulations of thermally driven disc winds in XRBs.

Since the code was originally described, significant improvements have been made over the years by, among others, Sim, Drew & Long (2005) and Matthews et al. (2015). We adopt the hybrid macro-atom scheme originally described by Matthews et al. (2015) for the models used here. Hydrogen and helium are treated in detail using the macro-atom formalism developed by Lucy (2002, 2003). Metals are treated as 'simple atoms' in which a two-level atom approximation is used to treat line interactions, and the treatment of the bound-free continuum is also simplified. Line transfer is treated in the Sobolev approximation, and strict radiative equilibrium (apart from a small cooling effect due to adiabatic cooling) is enforced in the comoving frame; as a result, all the reprocessed line and continuum emission discussed in Section 4.2 has its energetic origins in the input radiation sources (in this case, the accretion disc).

Our MCRT simulations assume an axisymmetric wind structure with reflective symmetry about the disc plane and cylindrical symmetry about the *z*-axis; however, MC photon packets are free to propagate in 3D. The density structure and velocity field throughout this axisymmetric outflow are determined using the kinematic prescription described below in Section 4.1.2. Once the density and velocity grid is specified, we aim to determine the effect of the outflow on the observed spectrum by using PYTHON to carry out the ionization and radiative transfer calculations. Detailed descriptions of how this works can be found in the references provided above. However, briefly, the calculations are carried out in two distinct stages. First, PYTHON generates sets of photon packets representing the radiation of all relevant system components over the full range of frequencies. Since we are only concerned with the soft state, the irradiated disc is currently the only component we consider in these simulations. These photon packets are followed as they make their way through the outflow and interact with the wind material. During this process, the ionization and temperature structure of the wind is iteratively updated until it converges. At this point, the ionization and temperature structures are frozen, and the calculation proceeds to the second stage, in which a detailed spectrum is calculated. Only photon packets in the spectral range of interest are generated at this stage.

4.1.1 Radiation sources

In order to model the X-shooter spectra of MAXI J1820+070, we assume that the accretion disc is optically thick and geometrically
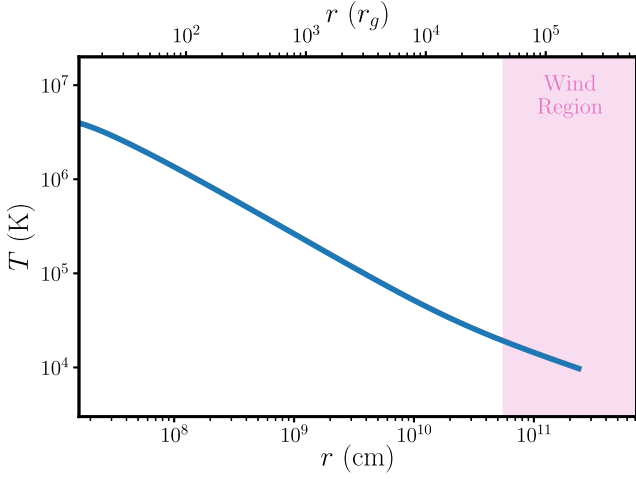
---

[5]PYTHON and is a collaborative open-source project available at https://github.com/agnwinds/python.

Figure 4. The temperature of the disc as a function of radius in our model. The pink-shaded region marks the approximate location of the disc wind, which has streamlines extending beyond the disc's outer edge.

thin. Its radiation field is then approximated by an ensemble of concentric annuli that emit blackbody radiation at the local disc temperature. The temperature profile we use is that suggested by the best-fitting full SED model described in Section 3.3. In the inner regions, viscous dissipation dominates, and $T_{visc}(r) \propto r^{-3/4}$; in the outer regions, irradiation dominates, flattening the temperature distribution to $T_{irr}(r) \propto r^{-3/7}$. The overall profile can be described by the sum $T^4(r) = T_{visc}^4(r) + T_{irr}^4(r)$, where

$$T_{visc}^4(r) = \frac{3GM_{BH}\dot{M}}{8\pi\sigma_{SB}r^3}, \tag{3}$$

and

$$T_{irr}^4(r) = \mathcal{C}(r)\frac{\dot{M}c^2}{4\pi\sigma_{SB}r^2}. \tag{4}$$

Here, G is the gravitational constant, $\dot{M}$ is the mass accretion rate, σ_{SB} is the Stefan–Boltzmann constant, and $\mathcal{C}(r)$ is the fraction of the luminosity ($L_X = \dot{M}c^2$) thermalized in the disc depending on the disc scale height and albedo. OPTXRPLIR parametrizes this as $\mathcal{C}(r) = (2/7)f_{out}(1 - a_{out})(r/r_{out})^{2/7}$, with the parameters and their values described in Section 3.3. The resulting temperature distribution is shown in Fig. 4.

4.1.2 Biconical wind model

We parametrize the wind as a biconical flow according to a prescription developed by Shlosman & Vitello (1993). We use this kinematic model because it is flexible and fairly simple and because we have developed a certain amount of insight into adjusting its parameters to produce synthetic spectra that resemble observations.

The Shlosman & Vitello (1993) model defines the wind in terms of streamlines that arise from the disc between the limiting radii r_{min} and r_{max}, with angles relative to the disc normal given by

$$\theta(r) = \theta_{min} + (\theta_{max} - \theta_{min})\left(\frac{r - r_{min}}{r_{max} - r_{min}}\right)^\gamma. \tag{5}$$

Here, θ_{min} and θ_{max} are the angles of the streamlines with respect to the polar axis at the inner and outer edge of the wind, and the exponent γ controls the concentration of streamlines. In our modelling here, we limit ourselves to the case $\gamma = 1$, so the streamlines are not concentrated toward the inner or outer edge of the flow.

Material flows along the streamlines according to a prescription that splits the velocity field into poloidal and azimuthal components. The poloidal velocity at a poloidal distance l along a streamline is given by

$$v_l(l) = v_0 + (v_\infty - v_0)\left(\frac{(l/R_v)^\alpha}{1 + (l/R_v)^\alpha}\right), \tag{6}$$

where R_v is an acceleration length (the point at which one reaches half the final velocity), v_0 is the initial velocity, v_∞, is the terminal velocity, and α determines the sharpness of the transition to high velocity. The azimuthal velocity, v_ϕ is set so that material in the wind initially rotates with the (Keplerian) disc but then conserves specific angular momentum. Thus, far from the disc's rotation axis, the wind's rotational velocity component, v_ϕ, is small.

Finally, to complete the description, one must define the mass outflow rate as a function of position. In the Shlosman & Vitello (1993) parametrization, the mass-loss rate per unit surface area, $\dot{m}$, is assumed to be given by

$$\dot{m} \propto \dot{M}_{wind}r^\lambda \cos(\theta(r)). \tag{7}$$

Here, $\dot{M}_{wind}$ is the total mass-loss rate carried by the outflow. For a narrow flow with θ_{min} not very different from θ_{max}, an exponent of $\lambda \simeq -2$ results in constant mass-loss rate as a function of the disc radius r. For the model, we ultimately found that for MAXI J1820+070, where θ_{max}, is close to 90°, mass-loss is concentrated toward r_{min}, because of the cosine term in the equation above.

4.1.3 Arriving at a fiducial model

Even though the Shlosman & Vitello (1993) prescription for an accretion disc wind is fairly simple, it involves quite a few tunable parameters. Given that the MCRT calculations require substantial computational resources, it is impractical to create a grid of models and to search a vast parameter space to find a 'best-fitting' model to an observed spectrum. Instead, our approach was to iterate from a set of parameters we consider physically plausible, adjusting one or two parameters at a time until we obtained spectra that look qualitatively similar to the observed spectrum of MAXI J1820+070 at about the proper distance and inclination.

The main characteristics of this model are inspired by recent radiation-hydrodynamical simulations of thermally driven disc winds in XRBs (e.g. Higginbottom & Proga 2015; Shidatsu et al. 2016; Higginbottom et al. 2018, 2020; Shidatsu et al. 2019). Thus, the outflow only begins at $r_{min} \simeq 10^5 R_g$, since thermal driving is only effective relatively far out in the disc (where the inverse Compton temperature – which is reached in the uppermost layers of the irradiated disc atmosphere – can exceed the escape speed). The adopted mass-loss rate in the model is $\dot{M}_{wind} = 10^{-8} \, \mathrm{M}_\odot \, \mathrm{yr}^{-1}$, which corresponds to about half of the accretion rate. This, too, is not unreasonable, both empirically (e.g. Ponti et al. 2012) and for a thermally driven wind (e.g. Higginbottom & Proga 2015; Shidatsu et al. 2016; Higginbottom et al. 2018, 2020; Shidatsu et al. 2019). To match the equatorially concentrated density structure of thermal disc winds, the inner and outer opening angles of the outflow have been set to 60° and 89.9°, respectively. However, the simulated spectra are fairly insensitive to this choice. The overall physical conditions throughout the fiducial model are discussed further in Section 4.2.3.

To obtain spectra that resembled MAXI J1820+070, we had to modify some of the wind parameters, particularly the initial velocity at the base of the streamlines, v_0, and the volume filling factor, f_V. Both of these parameters are important in dictating the density in the line-forming region and the overall reprocessing efficiency of

Table 4. Parameters of the fiducial wind model.

Parameter	Value	Comment
$\dot{M}_{\rm wind}$	$10^{-8}\,{\rm M_\odot\,yr^{-1}}$	Mass-loss rate
$r_{\rm min}$	$8900\,r_{\rm g}$	Inner edge of wind at base
$r_{\rm max}$	$12700\,r_{\rm g}$	Outer edge of wind at base
$\theta_{\rm min}$	$60°$	Angle of flow at inner wind edge
$\theta_{\rm max}$	$89.9°$	Angle of flow at outer wind edge
λ	-1	Mass-loss radial exponent
v_0	$1000\,{\rm cm\,s^{-1}}$	Velocity at base
$v_\infty(r)$	$1\,v_{\rm esc}(r)$	Terminal velocity
R_v	$5\times10^{11}\,{\rm cm}$	Acceleration length
α	2	Acceleration exponent
γ	1	Streamline skew
$f_{\rm V}$	0.02	Filling factor

the wind; however, they are also not unique in the sense that other parameters we did not adjust could have equal importance. We found we needed the material to be moderately clumpy, with a volume filling factor of $f_{\rm V} = 0.02$. The filling factor and mass-loss rate affect the results primarily via their ratio $\dot{M}_{\rm wind}/f_{\rm V}$, which helps to set the density in the line-forming region (see Section 4.2.4). Once we had arrived at a 'fiducial' model, we then explored changes in some of the other parameters to verify that the results were not locally very sensitive to them. However, we have not attempted to go beyond a general agreement between the model and the observed data. We comment further on the plausibility of clumping in the wind and the overall feasibility of line formation in the transition region of a disc wind, in Section 5.1. We have collated all the parameters of the fiducial wind model in Table 4.

4.2 Simulation results

4.2.1 Emission line spectrum

In Fig. 5, we compare our fiducial model to the observed spectrum of MAXI J1820+070. Since we are primarily interested in the emission line and photoionization edge signatures, we renormalize the model spectrum to match the data in each panel of the figure, i.e. in each wavelength region. The distances implied by this renormalization are indicated in the figure.

At a qualitative level, the simulated spectrum resembles that of MAXI J1820+070 at the time of the observations using the disc temperature profile that was generated to fit the multiwavelength SED. Most of the rich sets of double-peaked lines in the observed source also appear in the simulated spectrum. The normalization of the simulated spectrum correspond to a source at about the correct distance and inclination and the optical/IR continuum has about the correct slope due to a substantial contribution by free–free and bound–free emission from the wind region. The model spectrum approximately matches the strengths and widths of the observed hydrogen and helium features and the H and K lines of calcium. The most prominent lines missing from our model are the O III and N III Bowen lines near $\lambda 3450$ and $\lambda 4650$. These features are produced by fluorescence mechanisms not currently included in PYTHON.

Although the lines in both the observed and model spectra are double-peaked and of comparable width, there are interesting differences in the detailed line shapes; on the whole, the model lines seem to be fairly symmetric or to have stronger red than blue peaks, whereas the observed spectrum has lines in which the blue peak is brighter than the red peak. The asymmetry in the model line profile

is straightforward to understand. Most of the observed spectrum is generated by photons from a relatively thin layer above the near side of the disc; radiation associated with the back side of the disc is blocked by the disc itself. Photons produced in this layer can interact with material downstream in the outflow, moving toward the observer. As a result, any bound–bound absorption or scattering occurring in the outflow will preferentially affect the blue wings of the lines. If the spectrum produced by the emitting layer were flat or the line opacity higher, this would produce the classic blueshifted absorption signature associated with wind-formed P-Cygni profiles. However, the spectrum incident on the wind already contains strong and broad emission lines, so the absorption and scattering results only in the suppression of the blue line wings.

There are several possible explanations why the observed spectra do not show the same character, the most obvious being that the outflow was not axisymmetric at the time of these observations. The Keplerian period at the outer edge of the disc is almost 6 h, considerably longer than the time over which the spectra reported here were obtained. Given the relatively low velocities implied by the model we are using to simulate the spectra, it is also not clear that all of the wind is outflowing at all times. If we observe the system through gas settling onto the disc, one might expect the red peak to be stronger than the blue peak. In any event, we note that other spectra have been taken of MAXI J1820+070 in the same spectral state, showing brighter red peaks (Muñoz-Darias et al. 2019; Sánchez-Sierras & Muñoz-Darias 2020), so it is clear that the asymmetries are time variable.

4.2.2 Continuum emission and wind reprocessing

The overall slope of the spectrum shown in Fig. 5 roughly matches the observed continuum due to a significant amount of emission that arises in the wind, especially at the longer wavelengths. The model somewhat underpredicts the NIR flux, as indicated by the lower implied distance in this band. However, in the absence of reprocessed wind emission, the disc spectrum would have an even steeper spectral slope and underpredict the NIR flux more severely.

Wind reprocessing is an important factor in determining the emergent continuum in our modelling; this effect can be seen in Fig. 6, which shows the total broad-band SED escaping from our MCRT simulation, averaged over all viewing angles. We also show the input disc SED and escaping contributions from the disc and wind reprocessing. The escaping spectrum in the extreme-UV (EUV) and soft X-ray is largely unmodified, and the energy budget is dominated by the thermal bump from the hot irradiated disc, which peaks at $\approx 3 \times 10^{17}$ Hz as in Fig. 3. However, while the wind has a modest effect on the overall energetic output, the impact on the spectrum redward of the He II and Lyman edges – including in the X-Shooter region – is much more dramatic. The wind reprocesses the hot disc radiation into a quasi-thermal optical to near-infrared bump. Interestingly, the wind-processed continuum dominates over the disc radiation at the red end of the X-Shooter spectral region. In total, the wind absorbs around 3×10^{36} erg s^{-1} of the total luminosity, most of which is absorbed close to the peak of the SED, leading to a slight suppression of the X-rays and EUV which can barely be seen on the figure. This absorbed energy is radiated through a series of strong emission lines and recombination continua, and the wind noticeably changes the continuum slope in multiple wavebands. Thus, Fig. 6 shows that dense disc winds or disc atmospheres can have a dramatic impact on optical, UV, and NIR continua in XRBs, and possibly also
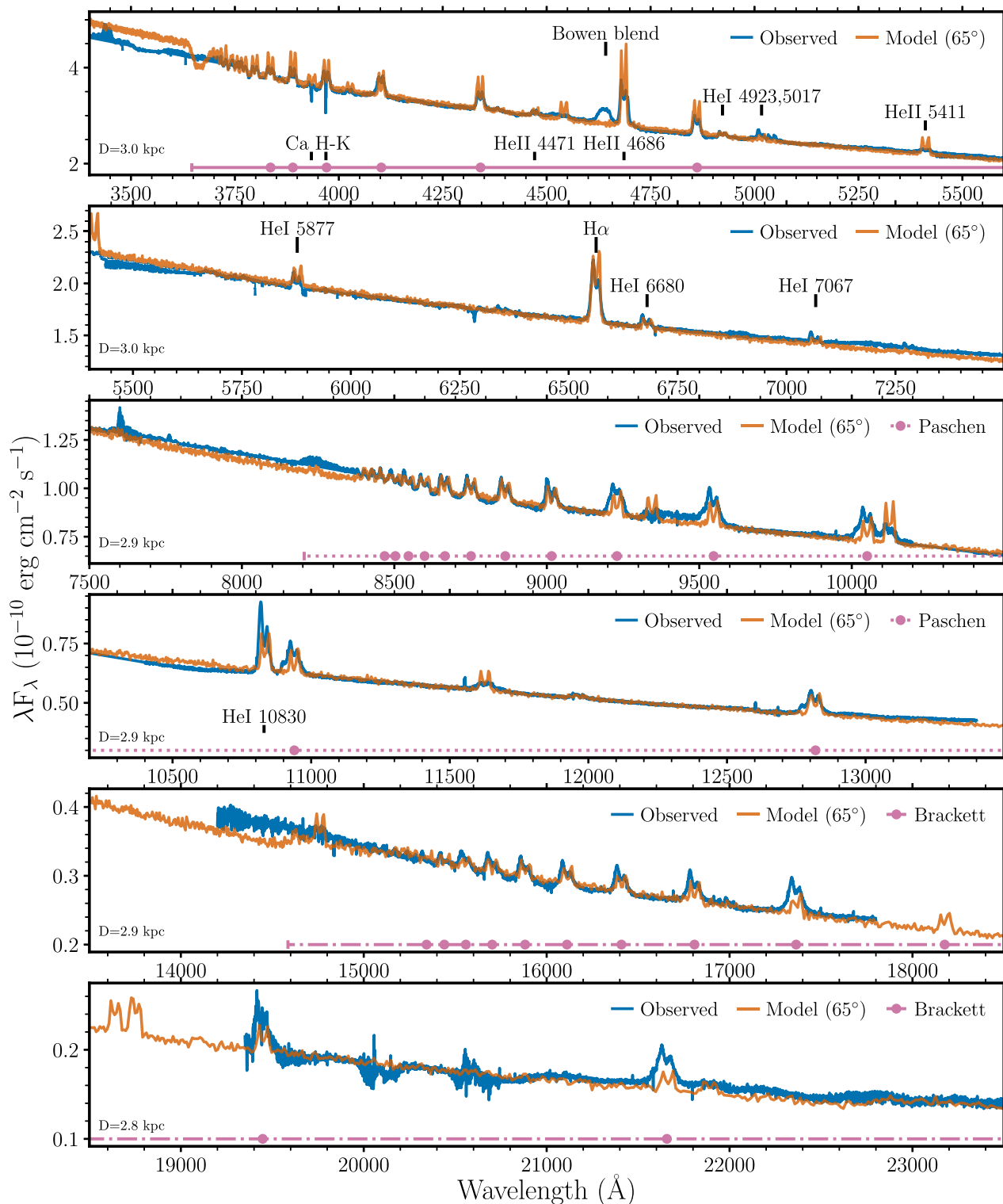
Figure 5. A comparison of the synthetic spectrum generated with our MCRT modelling to the observed spectrum of MAXI J1820+070. The synthetic spectra have been renormalized slightly to match the continuum and require a slightly different normalization at different wavelengths, reflecting a slight disagreement with the observed continuum shape. The prominent emission lines are marked, as are the Brackett and Paschen series. Except for the Bowen blend and higher order lines not captured by our atomic models, the wind model successfully produces *all* of the emission lines seen in the spectrum with similar shapes, equivalent widths, line widths, and relative intensities. There are some notable differences in the asymmetries of the emission lines, which are discussed in the text.
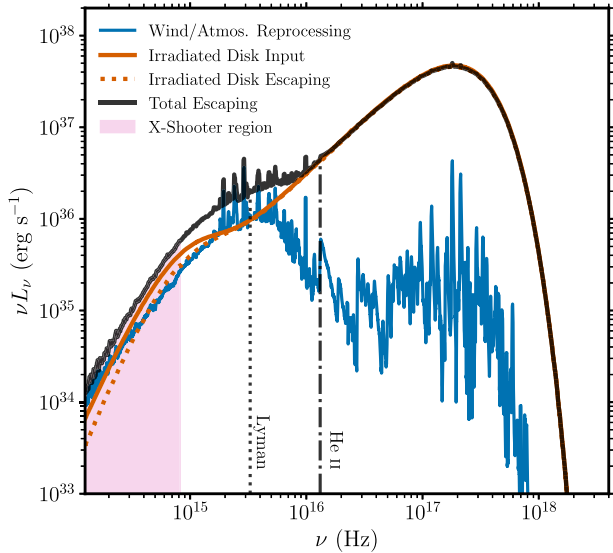
Figure 6. The broad-band spectral energy distribution obtained from the wind modelling and binned over all viewing angles. The total emergent spectrum is shown in black, the input irradiated disc spectrum in orange, and the spectrum produced by reprocessing in the wind in blue. The He II and Lyman ionization edges are marked, and so is the frequency region covered by the X-Shooter observations. The figure illustrates how the wind reprocesses the input radiation into continuum and line emission. Prominent recombination edges can be seen in the wind spectrum. The overall energetic output of the wind is small compared to the bolometric, but due to the spectral shape, this reprocessing still has a profound impact on the optical spectrum.

in other accreting systems (see e.g. Matthews et al. 2015; Parkinson et al. 2022).

Inspection of Fig. 5 shows that the shape of the continuum is not quite right close to the Balmer, Paschen, and Bracket limits (marked with vertical lines). Some of this effect, particularly at the Balmer limit, may be due to photoabsorption within the wind but could also be due to the limited number of levels used in our atomic model for hydrogen (up to a principal quantum number of 20). As a result, we do not include finely spaced lines very close to the ionization edge, which can form a pseudo-continuum leading up to the relevant limit. In particularly, the model includes 18 lines in the Balmer series, 17 in the Paschen series, and 16 in the Brackett series, which implies that regions of widths 36, 185, and 241 Å redward of the Balmer, Paschen, and Brackett limits, respectively, are not modelled accurately. In addition, in some of the included high-order lines, the line strengths will not be entirely accurate because radiative cascades from levels just above them are not included.

4.2.3 Physical properties of the fiducial wind model

The overall physical properties throughout the fiducial model are illustrated in Fig. 7, which shows the vertical wind velocity, v_z, ionization parameter, ξ, electron density, n_e and electron temperature, T_e, in the converged simulation. Fig. 7 demonstrates some of the overall characteristics of this roughly equatorial wind model. The wind base is dense, and a wedge-shaped region is formed, with aspect ratio $z/r \approx 0.2$, of moderate ionization material at temperatures conducive to forming hydrogen and helium recombination lines ($T_e \simeq 2$–4×10^4 K). The wind base is also subsonic, giving way to higher velocity, lower density material further out. In addition, the

upper layers of the wind are much hotter than the wind base, reaching maximum temperatures of $T_e \simeq 5 \times 10^5$ K.

In this type of wind model, the only natural location for forming optical lines is the base of the outflow, i.e. the interface between the relatively cool disc material close to the mid-plane and the X-ray-heated material at the top of the atmosphere. The transition region between these regimes is typically characterized by thermal instability, i.e. material moving upwards in the atmosphere tends to heat up extremely rapidly as it does so. Therefore, conditions suitable for forming optical lines are likely to be found in a fairly thin layer and relatively close to the mid-plane. As we shall see below (see Section 4.2.4), this is where most of the optical line formation takes place in our model.

However, it is important to remember that identifying the optical line-forming with, specifically, the base of a thermally driven wind is certainly not unique. *Any* layer above the disc plane with conditions similar to those found in our modelling would likely produce a similar optical emission line spectrum. This issue is discussed further in Section 5.1.

4.2.4 The line-forming region

In Fig. 8, we show the spatial distribution of line emissivities (as well as the H α/H β ratio discussed in Section 4.2.5) of some of the more prominent lines present in the modelled spectrum. The line emissivity here is the *local* line emissivity in a grid cell, in the sense that it includes, as a multiplicative factor, the Sobolev escape probability, but this does not mean this line emission necessarily escapes to the observer. We show these emissivities on logarithmic axes to show sufficient detail, but also show a reference plot on linear axes for comparison with Fig. 7. This choice of presentation is necessary because the line emission is produced relatively close to the disc. For example, 90 per cent of the H β emission is confined to $z < 10^4\ r_g$ ($z < 5 \times 10^{10}$ cm) and $z/r \lesssim 0.2$. Given the position of the emission, it is not surprising that the widths of the lines are very similar to the projected rotational velocity of the disc, which, for reference, is 625 km s^{-1} at the point where the X-ray illuminated disc ends.

The line formation region is inevitably stratified in terms of its physical properties (as is apparent from Figs 7 and 8), but it is none the less instructive to consider some characteristic physical conditions. We therefore order the simulation cells by a given physical quantity (n_e, T_e, and v_z) and calculate the cumulative distribution function (CDF) of the H β line luminosity in each case; the median (CDF = 0.5) value then gives us a reasonable characteristic value. This exercise reveals characteristic conditions in the H β line-forming region of $n_e \sim 10^{13}$ cm^{-3}, $T_e \sim 40\,000$ K and $v_z \sim 10$ km s^{-1}. This region can therefore be broadly characterized as a fairly thin wedge of dense, warm gas moving at subsonic to transonic velocities and is perhaps more accurately described as an atmosphere than a wind (see discussion in Section 5.1).

4.2.5 The Balmer decrement

The Balmer decrement describes the decreasing ratios of line intensities in the Balmer series, typically defined with respect to the intensity of H β (Burbidge & Burbidge 1953; Osterbrock & Ferland 2006). The Balmer decrement can be used to probe the physics of the line-emitting region by comparing the observed value to theoretical expectations. We calculated the Balmer decrement in MAXI J1820+070 from the continuum-subtracted line fluxes of
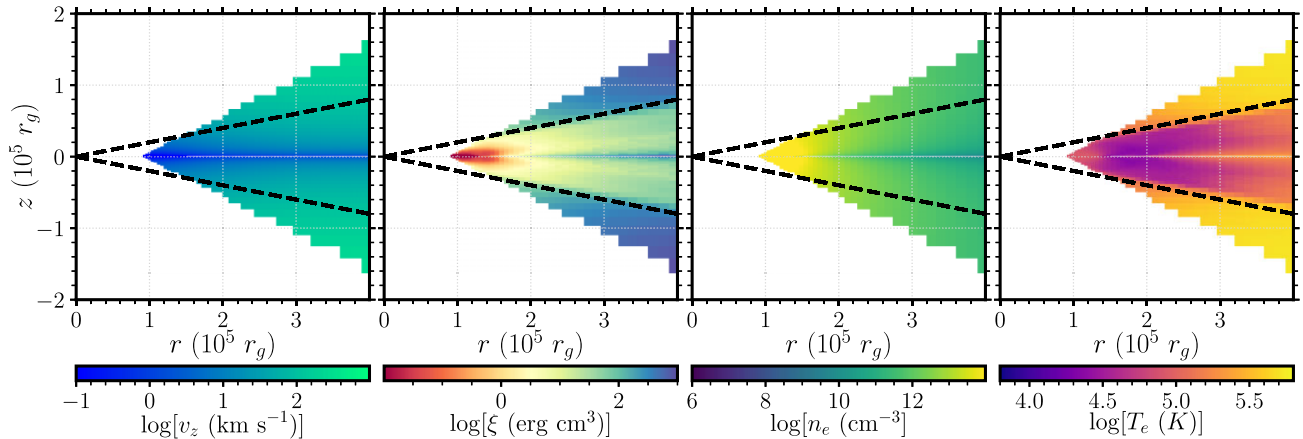
Figure 7. The physical conditions in the adopted wind model. The panels show, left to right, colour maps of logarithms of the vertical velocity component, v_z, the ionization parameter ξ, the electron density, n_e, and the electron temperature, T_e, for the wind used to produce the synthetic spectra shown in Fig. 5. The black dashed line shows a wedge with a scale height of $z/r = 0.2$. Only the region inside the disc radius is shown, but this is the source of essentially all of the line emission, and only the two positive $r \geq 0$ quadrants are plotted.

H α, H β, and H γ. The dereddened Balmer decrement in MAXI J1820+070 is rather flat, with H α/H $\beta \approx 1.3$ and H γ/H $\beta \approx 0.95$. These values are significantly lower than the canonical value of H α/H $\beta \approx 3$ expected from case B recombination theory (e.g. Osterbrock & Ferland 2006), and are more in line with case A recombination. These values also correspond to an emitting region temperature 10 000 K and a density of 2.5×10^{12} cm^{-3} using the model of Adams & Petrosian (1974).

Flat Balmer decrements have been observed in various astrophysical sources with several explanations proposed for their origin. For example, Williams (1980) find a flat Balmer decrement in CVs, proposing emission from a dense region near the disc, and similar proposals have been made for tidal disruption events (Short et al. 2020). In addition, a series of authors has calculated theoretical curves with varying assumptions about atomic physics and considering a range of physical conditions (density, temperature, optical depth, and ionizing radiation field). While the detailed behaviour depends on these parameters, the general trend is that the H α/H β can initially increase somewhat with density before decreasing to $\lesssim 1$ above $n_e \sim 10^{12}$–10^{13} cm^{-3} (Adams & Petrosian 1974; Drake & Ulrich 1980; Williams 1980). At these high densities, the lines can become optically thick, collisional de-excitations become important, and the H α/H β ratio is no longer set by the recombination rates. Instead, the level populations tend towards the local thermodynamic equilibrium (LTE) values at the local T_e. One caveat here is that radiative processes can also affect the Balmer decrement. For example, Elitzur (1984) highlights the importance of induced processes in intense radiation fields. In contrast, Ferland et al. (1982) show that flat Balmer decrements can be produced partly by stimulated emission, which drives the populations to LTE at lower densities.

To gain more insight and to examine the behaviour of the H α/H β ratio when the stratified wind structure is illuminated by a SED appropriate for MAXI J1820+070, we can examine the Balmer decrement from our MCRT modelling. In the bottom right-hand panel of Fig. 8, we show the H α/H β ratio throughout the wind. H α/H $\beta \lesssim 1$ in the dense base of the wind and throughout the majority of the line formation region. Higher up in the flow, the ratio increases, but we can also see the effect of Monte Carlo noise. In Fig. 9, we show the H α/H β ratio as a function of n_e from our MCRT wind modelling. Each point represents an individual grid cell and is colour

coded by temperature. Only cells that contribute at least 0.01 per cent of the total H α luminosity are plotted to illustrate the characteristic values in the line formation region. Additionally, we overlay three curves calculated with the photoionization code CLOUDY (Ferland et al. 1998, 2017). In the CLOUDY simulations, we considered a cloud of gas with a fixed column density of $N_H = 10^{23}$ cm^{-2} illuminated by the same irradiated disc SED that we use in our wind modelling. We placed the cloud at three different radii ($\log [r \text{ (cm)}] \in 11$, 11.5, 12) and calculated the H α/H β ratio at different densities n_e. The curves have a similar characteristic shape to the calculations presented in the literature mentioned above. However, the value of n_e at which the low H α/H β ratio regime is reached depends somewhat on the radius of the cloud (and therefore the dilution of the radiation field).

Our overall interpretation of the flat Balmer decrement in the emission line spectrum is similar to that of our MCRT wind modelling results. The flat Balmer decrement is consistent with emission from a dense wind base or disc atmosphere, a scenario that has also been suggested to explain the flat Balmer decrement in CVs (Williams 1980) and TDEs (Short et al. 2020). We discuss this scenario further in Section 5.1.

5 DISCUSSION

5.1 Optical line formation in the cool base of an X-ray heated wind or corona

A thermally driven outflow from an X-ray-heated accretion disc is not the most immediately promising environment for generating strong optical line emission. The conditions required to produce the observed hydrogen and helium recombination lines involve relatively low temperatures ($T \simeq 10^4$ K), moderate ionization, and relatively high densities. By contrast, thermal driving only takes off once material in the atmosphere is rapidly heated to near the inverse Compton temperature ($T_{IC} \simeq 10^6$–10^7 K), which happens at very high ionization parameters. Thus the rapidly outflowing material is unlikely to be a source of significant optical emission (unless it is exceptionally clumpy and/or multiple phases co-exist in the outflow).

In the context of a thermally driven wind model, this leaves the base of the outflow – i.e. the interface between the cool hydrostatic disc and the hot outflowing wind – as the most likely optical
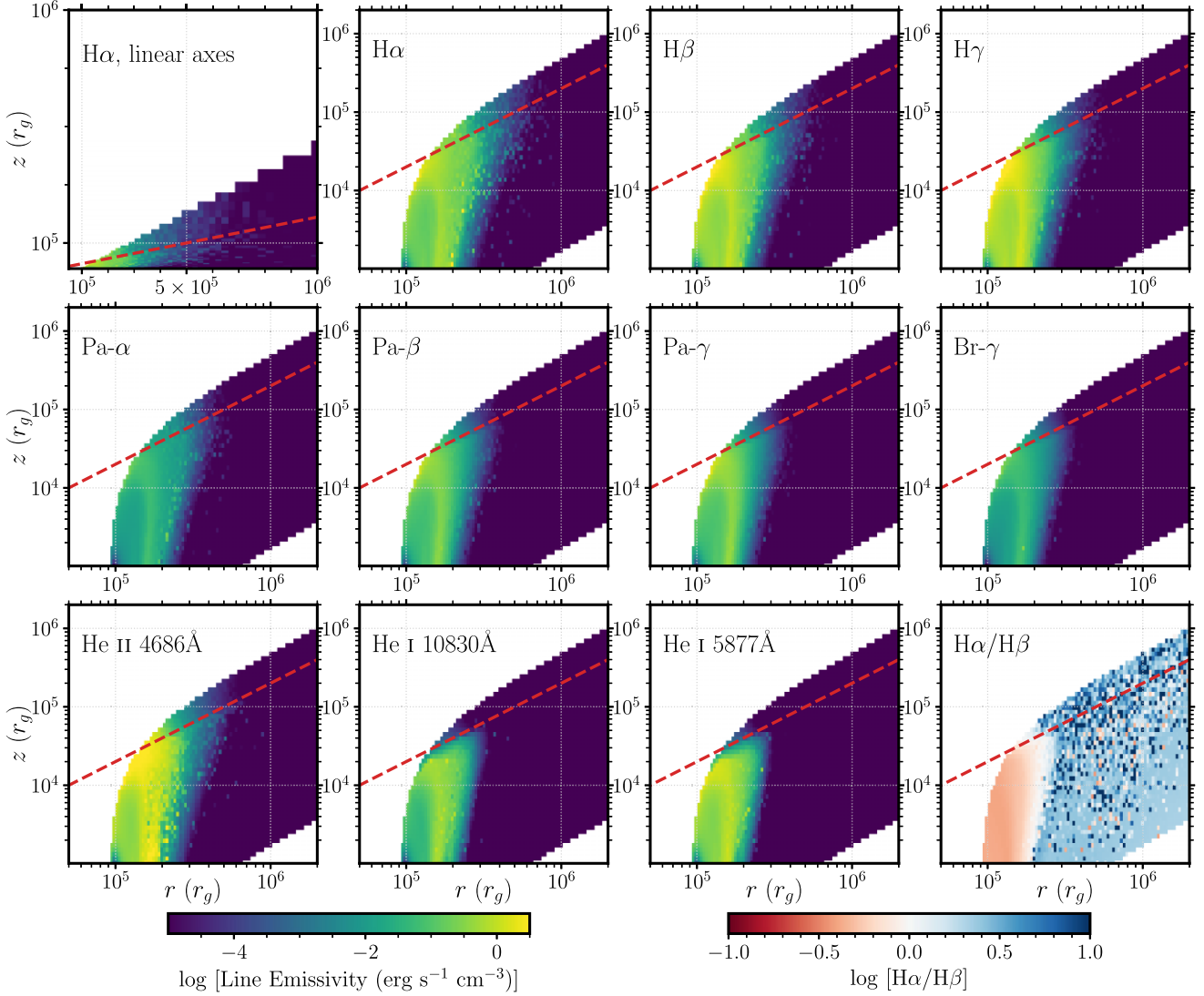
Figure 8. Various line emissivities throughout the wind. Line emissivities in each wind grid cell are plotted for some of the more prominent hydrogen and helium lines on a logarithmic spatial scale, except for the top left-hand panel, which shows a linear scale. The linear scale is plotted for easy comparison with Fig. 7 and to show the disc-like, flattened geometry of the line formation region. The red dashed line marks $z/r = 0.2$. The bottom-right-hand panel shows the H α/H β line ratio in the wind, which is relatively low ($\lesssim 1$) in the base of the wind but increases outwards as the density drops.

line-forming region. Are the properties of the line-forming region in our wind model consistent with such a scenario?

As already noted in Section 4.1.3, both the mass-loss rate ($\dot{M}_w \simeq \dot{M}_{\rm acc}$) and the location of the outflow on the disc ($R_{\rm min} \simeq 10^5 R_g$) in our model are reasonable for a thermally driven disc wind. We can estimate the density in the interface region between the hydrostatic disc and the outflow from the continuity equation. For simplicity, let us consider a quasi-spherical outflow starting at $R_0 \simeq R_{\rm min} \simeq 10^{11}$ cm with velocity $v_0 \simeq c_s$, where c_s is the sound speed at the base of the interface region. Temperatures here are of order 10^4 K, so we can write $c_s \simeq \sqrt{T/(10^4 \, \rm K)}$ km s^{-1}. Mass continuity then implies an initial density of

$$n_0 \sim \frac{\dot{M}_w}{f_V \, f_c \, 4\pi \, R_0^2 m_p v_0}, \tag{8}$$

where f_V is the filling factor, f_c is the covering factor, and $\dot{M}_w$ is the mass-loss rate of the wind. Plugging in numbers, we obtain a

characteristic value of

$$n_0 \sim 4 \times 10^{13} {\rm cm}^{-3} \left(\frac{\lambda_{{\rm Edd},w}}{f_V} \right) \left(\frac{f_c}{0.1} \right)^{-1} \left(\frac{v_0}{c_s} \right)^{-1}$$
$$\times \left(\frac{T_e}{10^4 {\rm K}} \right)^{-1/2} \left(\frac{r_0}{10^{11} {\rm cm}} \right)^{-2}, \tag{9}$$

where $\lambda_{{\rm Edd},w} = \dot{M}_w / \dot{M}_{\rm Edd}$ and f_V is the volume filling factor of the wind. Thus, we expect densities in this transonic region of the wind to be on the order of $\sim 10^{13}$ cm^{-3}. For reference, the density near the mid-plane of a standard Shakura–Sunyaev disc at $R \simeq 10^{11}$ cm is $\simeq 10^{15}$ cm^{-3} (Frank, King & Raine 2002).

We can now compare these numbers to the conditions found in the line-forming region of our fiducial wind model. These are illustrated in Fig. 10, which shows the local H β line luminosity as a function of both electron density, n_e, and vertical velocity, v_z. The location of $v = 10$ km s^{-1} (c_s at 10^4 K), $n_e = 10^{13}$ cm^{-3} is marked with a red cross, and is roughly coincident with the region of parameter space from which most of the H β line emission originates. These
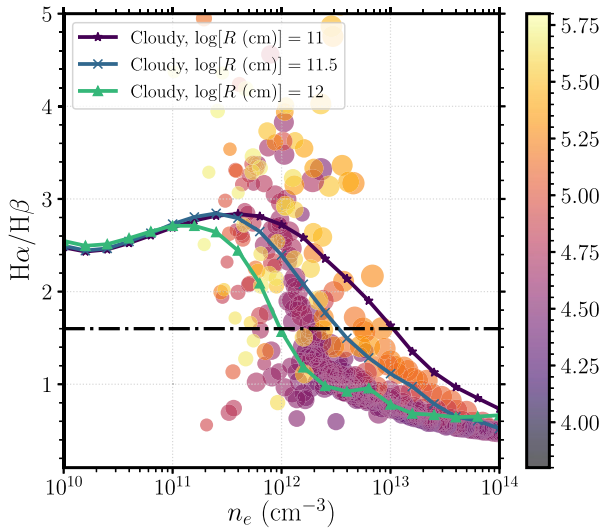
Figure 9. The Balmer decrement (H α/H β ratio) from our photoionization and radiative transfer modelling. The H α/H β ratio is plotted as a circle for every wind grid cell in the MCRT simulation, colour-coded by log [T_e (K)]. Three curves of H α/H β are overlaid from the CLOUDY simulations described in the text, and the dot–dashed line marks the inferred value of H α/H β = 1.3 from the observations for $E_{B-V} = 0.2$. Both codes independently find that $n_e \gtrsim 10^{12}$ cm^{-3} is needed to produce the observed flat Balmer decrement. However, material over a range of densities contributes to the line emission in the MCRT simulation.

Figure 10. An illustration of the location of the line formation region in velocity–density parameter space for our fiducial model showing that the H β line is formed in a transonic transition region between 'atmosphere' and 'wind'. For each point (corresponding to a wind grid cell), we plot the vertical velocity, v_z, against the electron density, n_e. The colour coding is set by the (logarithmic) local H β luminosity; as described in the text, this luminosity does not necessarily escape to infinity but does escape the local Sobolev zone. The horizontal dashed line marks the sound speed at 10^4 K, and the red cross marks the estimates of 'characteristic' conditions in the line formation region discussed in Sections 4.2.4 and 5.1.

conditions are also in line with our median estimates in Section 4.2.4 and the expectations from the flat Balmer decrement (Section 4.2.5). Thus, the physical conditions our model requires for the optical line-forming region are broadly consistent with those that might be expected in the transition region between the hydrostatic disc atmosphere and a thermally driven wind. To put it another way: our modelling implies that emission from the base of a thermally driven wind may self-consistently account for the recombination lines seen in the optical spectra of XRBs like MAXI J1820+070.

These results are promising, but it is also important to identify a few caveats. First, the association of the optical line-forming region with the base of a disc wind is not unique. Any model capable of generating similar physical conditions in the disc atmosphere will likely produce similar emission line spectra (e.g. from the temperature–inversion layer above an irradiated disc; Wu et al. 2001). After all, the optical line-forming region in our wind model lies well below the height at which material becomes unbound. Thus, the base of a hydrostatic vertically extended atmosphere could account for the observed spectrum. Indeed, the conditions in this layer may be broadly agnostic to what is happening higher up in the atmosphere. This final point is important for our second caveat: our fiducial model is somewhat different in terms of its temperature structure and volume filling factor from the smooth thermal wind model that inspired it. Specifically, the wind never quite reaches the high (Compton) temperatures ($T_e \gtrsim 10^6$ K) characteristic of the unbound supersonic flow in thermal winds (Begelman et al. 1983; Done, Tomaru & Takahashi 2018; Higginbottom et al. 2018). However, the details of this outer wind region do not determine the emission from the dense transition region below it, and our modelling does not rule out a hotter supersonic flow.

The above caveats are a useful reminder that what we *really* need at this point is a complete physical picture of the irradiated disc atmosphere, including its full radial and vertical structure. Developing
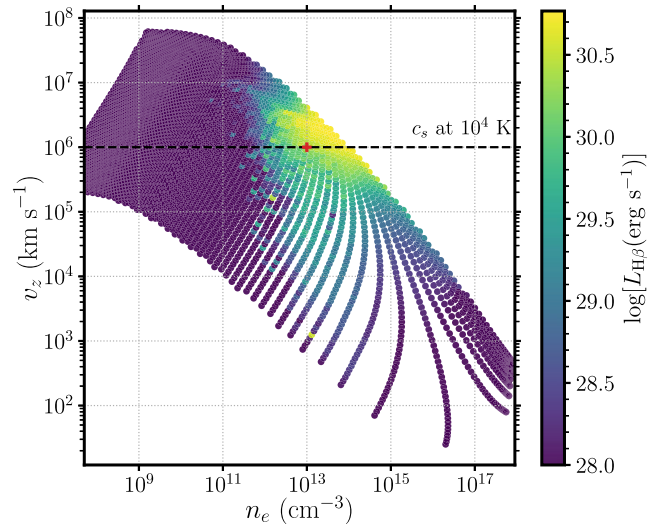
such a picture will require self-consistent radiation-hydrodynamic simulations akin to those carried out by Higginbottom et al. (2018, 2020), but including the physics needed to model the photosphere of the disc and covering the full range of relevant luminosities and spectral states. A particularly relevant study of X-ray-irradiated discs (Waters, Proga & Dannen 2021), shows that under certain conditions, the disc-wind transition region is far from smooth and is instead fragmented and clumpy due to thermal instability. Such a clumpy multiphase transition region is precisely the line-forming region supported by our model. It may also be important for generally explaining the optical wind absorption features in XRBs.

5.2 Implications for other X-ray binaries

Above, we have argued that the optical line emitting region may be a transition region between the disc atmosphere and the accretion disc wind. This is a promising identification since equatorial disc winds are thought to be associated with the soft X-ray states in XRB outbursts through the observations of highly ionized iron absorbers (Miller et al. 2006; Ponti et al. 2012). In addition, the observed conditions are in line with what has been seen in other XRBs. Flat Balmer decrements on the order of unity have been found earlier in the soft state of GX 339–4 (Rahoui et al. 2014) and Aql X–1 (Panizo-Espinar et al. 2021), suggesting high densities and the line widths of the emission lines are compatible with velocities of Keplerian orbits in the outer disc.

Based on our simulations, the flow has to be rather clumpy for the lines to arise from the transition region. This assumption is not unreasonable from a theoretical (Waters et al. 2021, see discussion in Section 5.1) or observational point of view. Considering the latter, in the high-inclination system Swift J1357.2−0933m fast variability optical dips were accompanied by blueshifted absorption troughs that can be attributed to a clumpy wind (Charles et al. 2019;
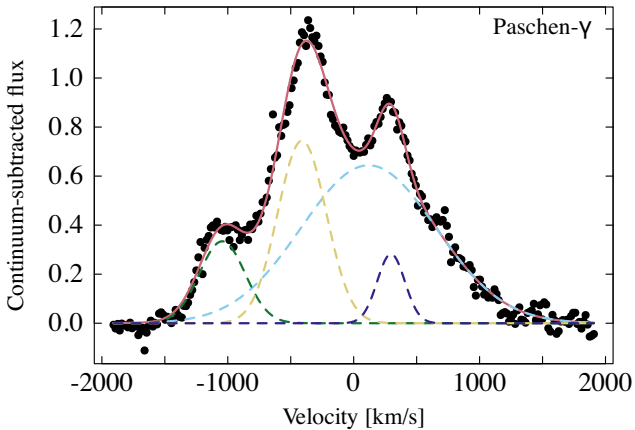
Figure 11. Continuum-subtracted line profile of the Paschen γ line at 10 938 Å. The profile can be fitted with four gaussian components indicating a complex line-emitting region.

Jiménez-Ibarra et al. 2019). Similar absorption troughs, although much narrower, have been observed in MAXI J1820+070 and MAXI J1348−630 (Panizo-Espinar et al. 2022). In MAXI J1820+070, wind features in the form of absorption troughs and extended emission line wings were found during the soft state in the infrared lines Pa γ and Pa β by Sánchez-Sierras & Muñoz-Darias (2020). They note that the increased level of ionization in the wind can cause the Balmer absorption profiles to disappear, while the Paschen series would be less affected. This scenario requires some mechanism to shield the strong X-ray emission from completely overionizing the wind. One possibility is having a clumpy and dense equatorial wind launched in the outer disc to retain suitable conditions for line formation.

As discussed in Section 4.2.1, the line profiles produced by our simulation qualitatively resemble the line profiles in the X-Shooter spectrum of MAXI J1820+070, but they do not produce them in detail. In part, this is because some of the profiles have multiple peaks. In Fig. 11, we plot the line profile of Pa γ from our X-Shooter observation. The profile is complex and can be fitted with four Gaussian components with varying velocities. Clearly, an azimuthally symmetric rotating region cannot be responsible for all components. Other XRBs with wind features in their spectra also tend to present excesses in the blue/red tails of the emission lines relative to a single Gaussian fit. In many cases, these wings are non-symmetric, with the blueshifted side dominating. This has been observed in J1803−298 (Mata Sánchez et al. 2022), GX 339−4 (Rahoui et al. 2014), and MAXI J1348−630 (Panizo-Espinar et al. 2022).

The observations of P-Cygni-like absorption profiles in the optical or near-infrared lines in systems with orbital inclinations surpassing 60 deg in the hard states of XRBs (Bandyopadhyay et al. 1997; Muñoz-Darias et al. 2016, 2017; Muñoz-Darias et al. 2018, 2019) indicate that the disc wind might be a more permanent structure in the evolution of XRB outbursts. What is changing is the amount of X-ray heating the outer disC due to changes in the geometry of the inner accretion flow between hard and soft states. This likely changes the temperature profile and the vertical structure of the outer disc with changing location and physical properties of the line-emitting region.

6 SUMMARY

We have analysed the optical/IR spectrum of the transient X-ray source MAXI J1820+070 as observed with X-Shooter on 2018-07-13 when the X-ray source was in the soft state and dominated

by emission from the disc. In order to carry out the analysis, we first presented the X-Shooter spectrum and used quasi-simultaneous *Swift*/UVOT, *NuSTAR*, and *NICER* data to construct the SED for the source. Then, based on relatively well-determined values of the mass, distance, reddening, and inclination, we developed a model of an X-ray illuminated disc that reproduces the SED of MAXI J1820+070 at the time of the X-Shooter observations. Finally, we used the implied temperature distribution as a function of radius as an input to simulate the optical/IR spectrum in terms of a biconical outflow from the surface of the disc. These simulations were performed with a Monte Carlo radiative transfer code capable of determining the ionization state and emergent spectrum of such systems. By adjusting the parameters of the model, we were able to generate simulated spectra that qualitatively resemble the observations (Fig. 5).

Our main conclusions are as follows:

(i) From a purely observational perspective, the optical/IR X-Shooter spectrum (Fig. 2) contains a rich collection of prominent primarily double-peaked emission lines associated with Balmer, Paschen, and Brackett series of hydrogen as well as various lines of singly and doubly ionized helium. Bowen fluorescence lines and the Ca II H&K lines are also readily apparent. However, we do not find prominent P-Cygni-like profiles that would be expected from a wind moving at velocities significantly greater than that expected from disc rotation.

(ii) The multiwavelength SED of MAXI J1820+070 in the soft state can be modelled with an irradiated disc, soft X-ray thermal component, and a broken power law to describe the UVOIR (Fig. 3). The latter components may arise from reprocessing in the wind or disc atmosphere. We did not find a suitable fit using only an irradiated disc component which underpredicted the near-infrared spectrum.

(iii) The optical/IR emission lines observed in MAXI J1820+070 arise in a dense region toward the outer disc (Fig. 8). In our modelling, the lines are formed in the dense base of a biconical disc wind, in a region characterized by $T_e \sim 40\,000$ K, $n_e \sim 10^{13}$ cm^{-3}, and outflow velocities close to the sound speed (Fig. 10). The emission line region has to be dense, independent of detailed modelling, because the ratio of the Balmer lines requires high density (Fig. 9). Any *outflow* (as opposed to rotational) velocities must be small in the line-forming region.

(iv) Much/most of the observed optical/IR continuum arises from the same region that produces the emission lines. At the densities required to produce the emission lines, free–free and free–bound emission comprise the bulk of the continuum, especially at longer wavelengths. Reprocessing by a wind or disc atmosphere can therefore have a profound effect on the optical (and even UV) continuum (Fig. 6) and can explain the near-infrared excess in our observation (although even with the reprocessing component the data is still somewhat underpredicted in the near-infrared). When emission lines of this strength are observed in other XRBs, it is important to be aware of this effect when deriving the temperature profile of the disc.

(v) Our modelling of the optical/IR emitting region in MAXI J1820+070 cannot distinguish whether it arises from an atmosphere or an accretion disc wind. Our parametrization for the wind does contain material moving at high velocity, but all of this material is too ionized and too tenuous to contribute to the optical/IR spectrum. Our modelling, combined with general estimates (Section 5.1), is still consistent with the optical line and continuum emission originating from the dense base of a thermal wind or perhaps from a clumpy unstable interface between the disc and wind. However, the optical/IR spectrum does not require the existence of fast, outflowing material.

Overall, our work demonstrates that the transition region between the disc atmosphere and a thermally driven wind can be the source of the rich optical line spectra seen in the soft states of X-ray binaries during outburst events. These *wind bases* can also dramatically impact the infrared-to-UV continua, even dominating the emission at the red part of the spectrum. With the ubiquity of accretion disc winds and strongly irradiated discs in many astrophysical sources, we suggest that these effects also apply to other X-ray binaries in addition to MAXI J1820+070, as well as other classes of accreting systems.

ACKNOWLEDGEMENTS

DATA AVAILABILITY

The VLT/X-Shooter data analysed here are available at the European Southern Observatory Science Archive Facility (http://archive.eso.org). UV and X-ray data are available at HEASARC. The simulation data produced as part of this work are available from the authors on request.

REFERENCES

Adams W. M., Petrosian V., 1974, ApJ, 192, 199
Allen J. L., Schulz N. S., Homan J., Neilsen J., Nowak M. A., Chakrabarty D., 2018, ApJ, 861, 26
Amôres E. B., Lépine J. R. D., 2005, AJ, 130, 659
Amôres E. B. et al., 2021, MNRAS, 508, 1788
Astropy Collaboration et al., 2013, A&A, 558, A33
Astropy Collaboration et al., 2018, AJ, 156, 123
Atri P. et al., 2020, MNRAS, 493, L81
Bandyopadhyay R., Shahbaz T., Charles P. A., van Kerkwijk M. H., Naylor T., 1997, MNRAS, 285, 718
Begelman M. C., McKee C. F., Shields G. A., 1983, ApJ, 271, 70
Bianchi S., Ponti G., Muñoz-Darias T., Petrucci P.-O., 2017, MNRAS, 472, 2454
Bohlin R. C., Savage B. D., Drake J. F., 1978, ApJ, 224, 132
Burbidge G. R., Burbidge E. M., 1953, ApJ, 118, 252
Cardelli J. A., Clayton G. C., Mathis J. S., 1989, ApJ, 345, 245

Casares J., Muñoz-Darias T., Mata Sánchez D., Charles P. A., Torres M. A. P., Armas Padilla M., Fender R. P., García-Rojas J., 2019, MNRAS, 488, 1356
Castro Segura N. et al., 2022, Nature, 603, 52
Chakravorty S., Lee J. C., Neilsen J., 2013, MNRAS, 436, 560
Charles P., Matthews J. H., Buckley D. A. H., Gandhi P., Kotze E., Paice J., 2019, MNRAS, 489, L47
Chiang C. Y., Done C., Still M., Godet O., 2010, MNRAS, 403, 1102
Davis S. W., Blaes O. M., Hubeny I., Turner N. J., 2005, ApJ, 621, 372
Díaz Trigo M., Boirin L., 2016, Astron. Nachr., 337, 368
Díaz Trigo M., Sidoli L., Boirin L., Parmar A. N., 2012, A&A, 543, A50
Díaz Trigo M., Migliari S., Miller-Jones J. C. A., Guainazzi M., 2014, A&A, 571, A76
Done C., Davis S. W., Jin C., Blaes O., Ward M., 2012, MNRAS, 420, 1848
Done C., Tomaru R., Takahashi T., 2018, MNRAS, 473, 838
Drake S. A., Ulrich R. K., 1980, ApJS, 42, 351
Drimmel R., Cabrera-Lavers A., López-Corredoira M., 2003, A&A, 409, 205
Elitzur M., 1984, ApJ, 280, 653
Fabian A. C. et al., 2020, MNRAS, 493, 5389
Fender R. P., Belloni T. M., Gallo E., 2004, MNRAS, 355, 1105
Ferland G. J., Lambert D. L., McCall M. L., Shields G. A., Slovak M. H., 1982, ApJ, 260, 794
Ferland G. J., Korista K. T., Verner D. A., Ferguson J. W., Kingdon J. B., Verner E. M., 1998, PASP, 110, 761
Ferland G. J. et al., 2017, RMxAA, 53, 385
Frank J., King A., Raine D. J., 2002, Accretion Power in Astrophysics, 3rd edn. Cambridge Univ. Press, Cambridge
Friedman S. D. et al., 2011, ApJ, 727, 33
Gabriel E. et al., 2004, in Proceedings, 11th European PVM/MPI Users' Group Meeting. Budapest, Hungary, p. 97
Gierliński M., Done C., Page K., 2009, MNRAS, 392, 1106
Green G. M. et al., 2018, MNRAS, 478, 651
Guan J. et al., 2021, MNRAS, 504, 2168
HI4PI Collaboration et al., 2016, A&A, 594, A116
Haardt F., Maraschi L., Ghisellini G., 1994, ApJ, 432, L95
Higginbottom N., Proga D., 2015, ApJ, 807, 107
Higginbottom N., Knigge C., Long K. S., Matthews J. H., Sim S. A., Hewitt H. A., 2018, MNRAS, 479, 3651
Higginbottom N., Knigge C., Long K. S., Matthews J. H., Parkinson E. J., 2019, MNRAS, 484, 4635
Higginbottom N., Knigge C., Sim S. A., Long K. S., Matthews J. H., Hewitt H. A., Parkinson E. J., Mangham S. W., 2020, MNRAS, 492, 5271
Homan J., Neilsen J., Allen J. L., Chakrabarty D., Fender R., Fridriksson J. K., Remillard R. A., Schulz N., 2016, ApJ, 830, L5
Hunter J. D., 2007, Comput. Sci. Eng., 9, 90
Jimenez-Garate M. A., Raymond J. C., Liedahl D. A., Hailey C. J., 2001, ApJ, 558, 448
Jimenez-Garate M. A., Raymond J. C., Liedahl D. A., 2002, ApJ, 581, 1297
Jiménez-Ibarra F., Muñoz-Darias T., Casares J., Armas Padilla M., Corral-Santana J. M., 2019, MNRAS, 489, 3420
Kimura M., Done C., 2019, MNRAS, 482, 626
Liszt H., 2014, ApJ, 783, 17
Long K. S., Knigge C., 2002, ApJ, 579, 725
Lucy L. B., 2002, A&A, 384, 725
Lucy L. B., 2003, A&A, 403, 261
Mata Sánchez D. et al., 2022, ApJ, 926, L10
Matthews J. H., Knigge C., Long K. S., Sim S. A., Higginbottom N., 2015, MNRAS, 450, 3331
Miller J. M. et al., 2006, ApJ, 646, 394
Miller J. M. et al., 2012, ApJ, 759, L6
Muñoz-Darias T. et al., 2016, Nature, 534, 75
Muñoz-Darias T. et al., 2017, MNRAS, 465, L124
Muñoz-Darias T., Torres M. A. P., Garcia M. R., 2018, MNRAS, 479, 3987
Muñoz-Darias T. et al., 2019, ApJ, 879, L4
Neilsen J., Lee J. C., 2009, Nature, 458, 481
Neilsen J., Remillard R. A., Lee J. C., 2011, ApJ, 737, 69
Osterbrock D. E., Ferland G. J., 2006, Astrophysics of gaseous nebulae and active galactic nuclei. University Science Books, Sausalito, CA

Panizo-Espinar G., Muñoz-Darias T., Armas Padilla M., Jiménez-Ibarra F., Casares J., Mata Sánchez D., 2021, A&A, 650, A135

Panizo-Espinar G. et al., 2022, A&A, 664, 9

Parkinson E. J., Knigge C., Matthews J. H., Long K. S., Higginbottom N., Sim S. A., Mangham S. W., 2022, MNRAS, 510, 5426

Planck Collaboration XI 2014, A&A, 571, A11

Ponti G., Fender R. P., Begelman M. C., Dunn R. J. H., Neilsen J., Coriat M., 2012, MNRAS, 422, L11

Ponti G., Muñoz-Darias T., Fender R. P., 2014, MNRAS, 444, 1829

Ponti G., Bianchi S., Muñoz-Darias T., De K., Fender R., Merloni A., 2016, Astron. Nachr., 337, 512

Proga D., Kallman T. R., 2002, ApJ, 565, 455

Rahoui F., Coriat M., Lee J. C., 2014, MNRAS, 442, 1610

Sánchez-Sierras J., Muñoz-Darias T., 2020, A&A, 640, L3

Schlafly E. F. et al., 2014, ApJ, 789, 15

Shaw A. W. et al., 2016, MNRAS, 458, 1636

Shidatsu M., Done C., Ueda Y., 2016, ApJ, 823, 159

Shidatsu M., Nakahira S., Murata K. L., Adachi R., Kawai N., Ueda Y., Negoro H., 2019, ApJ, 874, 183

Shlosman I., Vitello P., 1993, ApJ, 409, 372

Short P. et al., 2020, MNRAS, 498, 4119

Sim S. A., Drew J. E., Long K. S., 2005, MNRAS, 363, 615

Smette A. et al., 2015, A&A, 576, A77

Tetarenko B. E., Dubus G., Lasota J. P., Heinke C. O., Sivakoff G. R., 2018, MNRAS, 480, 2

Torres M. A. P., Casares J., Jiménez-Ibarra F., Álvarez-Hernández A., Muñoz-Darias T., Armas Padilla M., Jonker P. G., Heida M., 2020, ApJ, 893, L37

Tucker M. A. et al., 2018, ApJ, 867, L9

Ueda Y. et al., 2010, ApJ, 713, 257

van Paradijs J., McClintock J. E., 1994, A&A, 290, 133

Virtanen P. et al., 2020, Nat. Methods, 17, 261

Waters T., Proga D., Dannen R., 2021, ApJ, 914, 62

Williams R. E., 1980, ApJ, 235, 939

Wilms J., Allen A., McCray R., 2000, ApJ, 542, 914

Woods D. T., Klein R. I., Castor J. I., McKee C. F., Bell J. B., 1996, ApJ, 461, 767

Wu K., Soria R., Hunstead R. W., Johnston H. M., 2001, MNRAS, 320, 177

Zhao X. et al., 2021, ApJ, 916, 108

Zhu Y., Davis S. W., Narayan R., Kulkarni A. K., Penna R. F., McClintock J. E., 2012, MNRAS, 424, 2504

Życki P. T., Done C., Smith D. A., 2001, MNRAS, 326, 1367

This paper has been typeset from a TEX/LATEX file prepared by the author.